Tidal effects in a realistic model of a thermally buoyant plume north of Pt. Conception

Sutara Suanda[1], Presenting Author, Nirnimesh Kumar[1], Arthur J. Miller[1], Emanuele Di Lorenzo[2], Kevin Haas[2], Donghua Cai[2], Christopher A. Edwards[3], and Falk Feddersen[1]

[1]Scripps Institution of Oceanography, University of California San Diego
ssuanda@ucsd.edu
[2] Georgia Institute of Technology
[3]University of California Santa Cruz

Abstract

A multi-nested Regional Ocean Modeling System (ROMS) simulates observed water column temperature increases due to a thermally-buoyant plume. A mean temperature bias is the dominant source of model-data mismatch which is reduced by inclusion of tidal forcing. Model temperature diagnostics are used to identify the bulk mechanisms by which tidal processes affect temperature evolution. Integrated over the entire shelf region, the increase in vertical mixing is small relative to the decrease in lateral boundary advective heat fluxes in the tidal simulation. With tides, advective heat fluxes are reduced due to a combination of a decrease in mean advective heat flux and tidal correlations, which account for a net cooling of the continental shelf during thermal plume events.

1 Introduction

Near Pt. Conception, California (Fig. 1), the coastal ocean response to wind relaxations is dominated by the poleward propagation of relatively warm Santa Barbara Channel (SBC) water (Melton et al., 2009; Washburn et al., 2011). Historical observations show that these relaxation flows are kinematically consistent with a thermally buoyant plume, and are an important transport mechanism of SBC water to the continental shelf north of Pt. Conception. Although the buoyant plume is primarily controlled by low-frequency continental shelf processes such as winds and large-scale pressure gradients, the effect of barotropic and baroclinic tides on plume structure and temperature transport is relatively unknown.

A multi-nested realistic regional coastal ocean model is configured with daily-averaged surface forcing, large-scale lateral boundary forcing, as well as the inclusion of tides and surface gravity waves (Suanda et al., 2016). Previously these types of models have been shown to reproduce well the statistics of subtidal and tidal band fluctuations across the continental shelf (*e.g.,* Kumar et al., 2016). Through analysis of model diagnostic fields, the goal of this contribution is to further understand the temperature dynamics associated with the Pt. Conception plume and the implications of the addition of tides. The model setup is briefly described (further details in Suanda et al. (2016)), followed by an examination of the modeled plume. Differences in the temperature diagnostic fields between the tide and no tide simulations are presented and discussed.

2 ROMS

The model is the Rutgers Regional Ocean Modeling System (ROMS), a three-dimensional, terrain-following numerical model solving the Reynolds-averaged Navier-Stokes equations

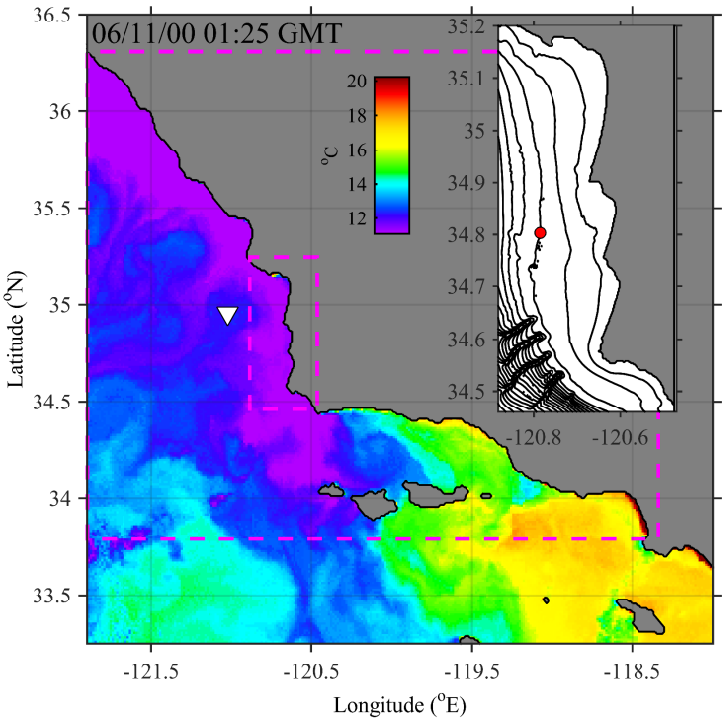

Figure 1: Advanced Very High resolution Radiometer (AVHRR) image of sea surface temperature (11 June, 2000). White triangle denotes location of NDBC buoy 46011. The outer magenta box delineates the Δx = 600 m nest. The inner magenta box denotes the Δx = 200 m grid. Inset zooms to shelf bathymetry from the Δx = 200 m grid. Red dot denotes the location of a mooring used for model-data comparison (100-m water depth).

with hydrostatic and Boussinesq approximations (Shchepetkin and McWilliams, 2005; Warner et al., 2010). A series of nested one-way simulations are run where the largest relevant forcing scales are simulated on a coarse grid and variability is transmitted to smaller domains of higher horizontal resolution through open boundary conditions (downscaling). At these higher levels of nesting, additional smaller-scale forcing mechanisms (*i.e.*, tides) are then added.

The outermost model (Δx = 3 km), extends from the Baja peninsula to Washington State encompassing the eastern Pacific basin. Nested simulations discussed in this contribution will include results from two grids Δx = 600 m and Δx = 200 m (Fig. 1). Model bathymetry and coastline resolution (https://www.ngdc.noaa.gov/) are increased at each level of nesting. Simulations have 42 vertical levels, and use the Generic Length Scale (GLS) vertical mixing scheme with $k-\omega$ parameters to solve for vertical eddy viscosity and diffusivity. Radiation boundary conditions are applied to barotropic fields to allow outgoing energy (Chapman, 1985; Flather, 1976; Mason et al., 2010), and both radiation and nudging are used for baroclinic boundary conditions (Marchesiello et al., 2001).

To downscale simulations, sea level, tracer, and momentum fields are interpolated at each time step to the grid boundaries (boundary conditions) and to interior grid points for the first time step (initial conditions) of the nested simulation. All simulations are forced at the surface with atmospheric variables (wind, air temperature, pressure, relative humidity, and incoming solar radiation) output from the Coupled Ocean-Atmosphere Mesoscale Prediction System (COAMPS) model (Hodur et al., 2002). COAMPS output (9 km

horizontal resolution) are daily-averaged and interpolated to higher horizontal resolution for nested ROMS simulations. For simulations with tides, tidal harmonic sea level and barotropic velocities from eight astronomical tidal constituents (K_2, S_2, M_2, N_2, K_1, P_1, O_1, Q_1) are applied as boundary forcing on the Δx = 600 m grid from the ADCIRC tidal model (Mark et al., 2004).

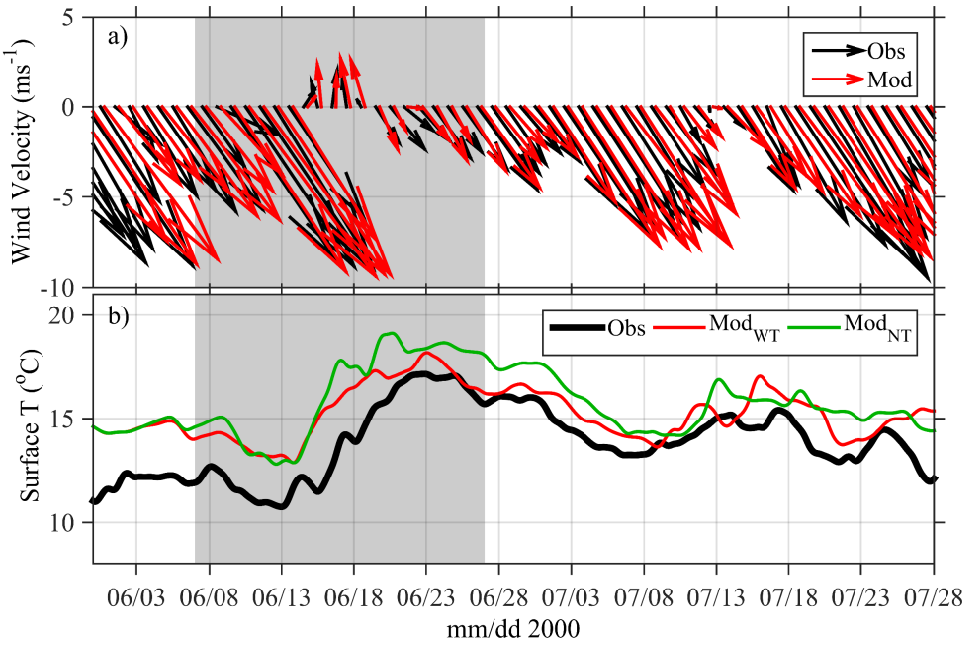

Figure 2: Time series model-data comparison. a) Observed daily-averaged (black) and modeled (red) winds at NDBC 46011. b) Observed sub-tidal surface temperature at 100 m mooring (thick black) compared to modeled sub-tidal time series from with tide (red) and no tide (green) simulations. In both panels, the period of heat budget analysis is shaded gray.

3 Results

In the following, Δx = 200 m grid simulations are compared with the inclusion of tidal forcing (WT) to those without tidal forcing (NT). During the study period, model winds are consistent with those observed (Fig. 2 a). The relaxation and reversal of the mostly upwelling-favorable winds coincides with the largest sub-tidal (33-hour filtered) warming signal ($\sim$ 5°C) observed in the surface at the 100-m mooring (Fig. 2 b). Both modeled sub-tidal time series are similar to those observed (a complete model-data comparison and discussion of the high model bias is given in Suanda et al. (2016)), however modeled surface temperature is 0.5°C smaller, and better compares with observations in the WT simulation.

Between the two simulations, model sea surface temperature (SST) snapshots show a similar progression as the warm water plume propagates northward (Fig. 3). Before the plume arrives, the signature of coastal upwelling can be seen in both images. Two days later, warm SBC water rounds Pt. Conception and propagates poleward. Finally, SBC water dominates the SST signal on the shelf in this location. The shelf remains warm for a number of days after the plume front passes and coastal upwelling resumes (not shown). While the speed of warm water propagation and overall structures are fairly

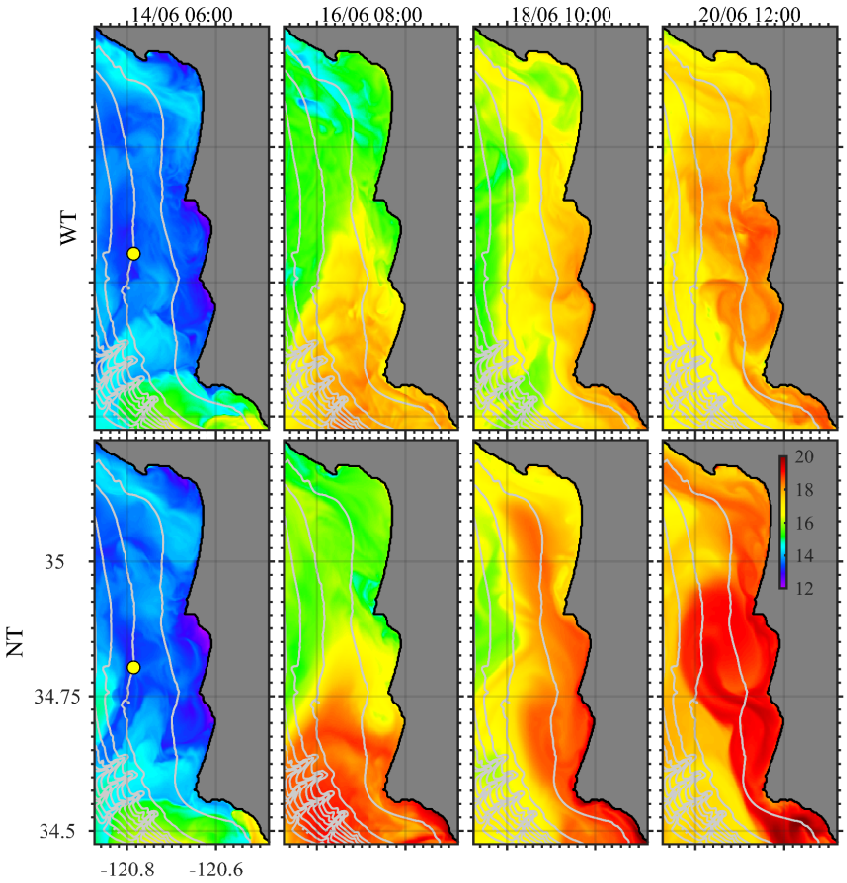

Figure 3: Four snaphots of modeled SST from the with tide (WT) simulation (top panels) and no tide (NT) simulation (bottom panels). Snapshote are from the same time in both simulations, with 2 day spacing. Isobath contours are in 50-m increments, yellow dot shows location of 100-m mooring.

similar between the two simulations, smaller-scale spatial structures associated with the tides are seen in the WT snapshots.

3.1 Temperature Diagnostics

Temperature dynamics during the thermal plume and differences in the NT and WT simulations are further investigated with the model diagnostic of the heat equation:

$$\frac{\partial T}{\partial t} = -\nabla.\left(\mathbf{u}T\right) + \frac{\partial}{\partial z}K_t\frac{\partial T}{\partial z}. \tag{1}$$

Here, the left-hand-side of Eq. 1 represents the time rate of change of temperature stored (Sto). Terms on the right-hand-side of Eq. 1 are the divergence of advective heat fluxes (Adv), and the vertical gradient of a turbulent heat flux with diffusivity K_t calculated by model turbulence closure (Mix). Model diagnostics also include the divergence of horizontal turbulent fluxes, but these are small compared to the terms in Eq. 1 and are ignored.

Using time-varying thickness of each modeled grid cell, Eq. 1 terms are volume-integrated over the entire Δx = 200 m computational domain,

$$\int_V \frac{\partial T}{\partial t}dV = -\int_V \nabla.\left(\mathbf{u}T\right)dV + \int_V \frac{\partial}{\partial z}K_t\frac{\partial T}{\partial z}dV. \tag{2}$$

Equation 2 expresses the total volume-integrated time rate of change of temperature storage is equal to the sum of the advective temperature flux through the lateral (western and southern) boundaries and the integrated vertical mixing. Vertically integrated mixing is related to the surface heat flux because of the surface boundary condition (at $z = 0$) for temperature,

$$K_t \frac{\partial T}{\partial z}|_{z=0} = \frac{Q_0}{\rho c_p} \tag{3}$$

where Q_0 is the net surface heat flux.

Table 1: The mean and standard deviation of terms in the volume-integrated heat budget (Eq. 2) reported with units of $^{o}\mathrm{Cm}^3\mathrm{s}^{-1}$.

WT	**Mean** (10^5)	**Std** (10^6)
Sto	2.52	1.16
Adv	1.56	1.16
Mix	0.94	0.02
NT	**Mean** (10^5)	**Std** (10^6)
Sto	3.59	0.13
Adv	2.68	0.12
Mix	0.90	0.02

During the plume period, the mean and standard deviation of boundary temperature advection is a larger contributor to the volume-integrated temperature storage compared to the mixing term in both WT and NT simulations (Table 1). Due to tidal variability, the standard deviation in boundary flux of the WT simulation increases by an order of magnitude relative to the NT simulation. However, in the time-mean, both the storage and boundary advection terms are smaller in the WT relative to NT simulations.

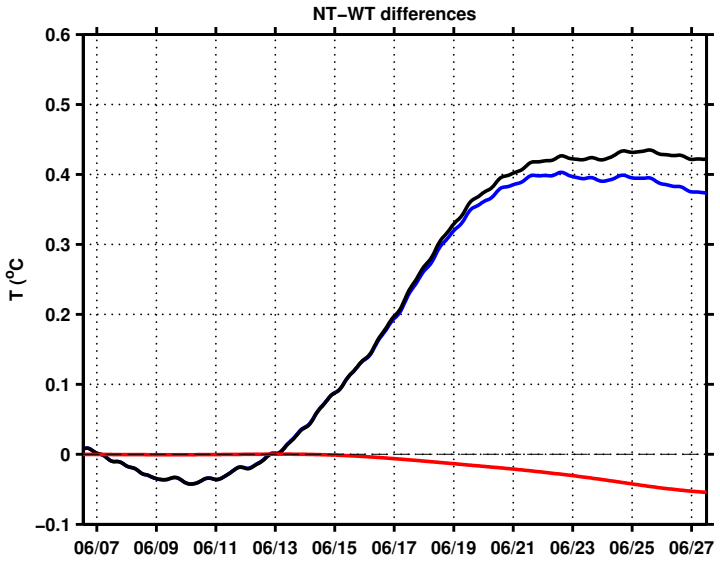

Figure 4: Time-integrated terms in the volume-averaged heat budget. Terms are the time-integrated heat storage (blue), lateral advection (black), and vertical mixing (red).

Alternatively, WT and NT differences are seen by temporally integrating the terms in Eq. 2 and taking a volume-average, giving an average change in shelf temperature during

the plume period (*e.g.,* Wilkin, 2006). The difference between the two time integrals shows that the average temperature increase across the entire shelf due to the plume is about 0.4 °C larger in the NT simulation (Fig. 4). Again, these changes are dominated by the decrease in advective boundary fluxes during this period.

4 Discussion

The addition of tides results in a small increase in the vertical mixing term. Because it is vertically integrated, the increase in vertical mixing amounts to an increase in surface heat flux Q_0 in the WT simulation. The net surface heat flux can be written as the sum of the incoming shortwave minus the sensible, latent and net-long wave heat losses, $Q_0 = Q_{sw} - (Q_{sens} + Q_{lat} + Q_{nlw})$ (Gill, 1982). Using the SST difference of 0.5° in the WT simulation, we estimate that the feedback between this SST difference and the sensible, latent and net-long wave heat losses are indeed enough to account for the net surface heat flux increase of 5 - 8% in the WT simulations.

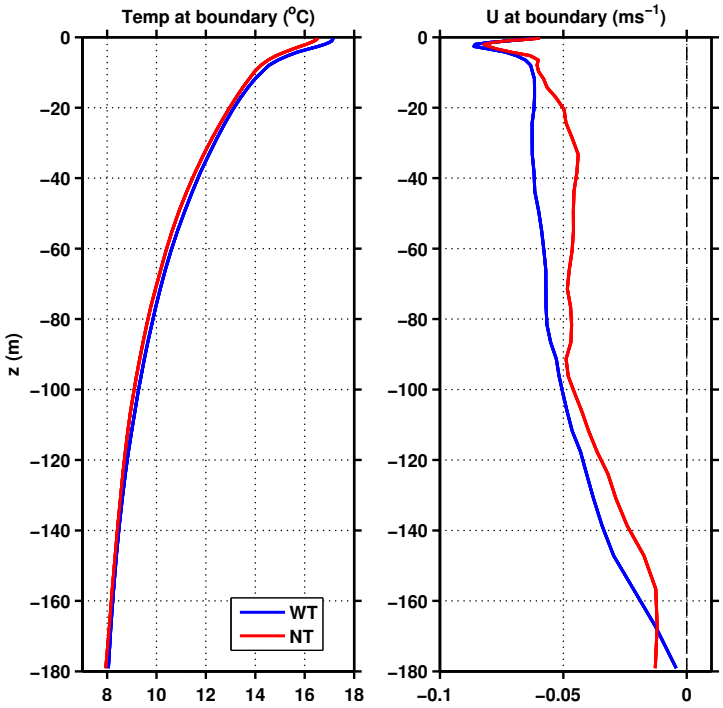

Figure 5: Profiles of relaxation event (June 12 - 19) mean temperature (left) and east-west oriented velocity at the offshore boundary of the 200m grid domain boundary. Velocity is slightly reduced while, temperature is nearly identical except near the surface.

How are advective heat fluxes altered with the addition of tides? We first assume that the boundary-normal velocity and temperature at the boundary can be decomposed such that:

$$\langle uT \rangle = \langle \overline{u}\,\overline{T} \rangle + \langle u'T' \rangle, \tag{4}$$

where angled-brackets denote a time mean and the subscript overbar denotes a sub-tidal signal. If the low-frequency signal is similar between the WT and NT simulations, the decrease in advective heat flux implies that the tidal correlation term $\langle u'T' \rangle$ is a net cooling. To confirm that the sub-tidal boundary temperature and velocity signal is similar between the WT and NT simulations, profiles of low-fequency temperature and velocity

are compared (Fig. 5). The profiles are fairly similar, somewhat confirming this assertion. Additionally, the differences are confined to the near-surface, suggesting that overall plume kinematics are not much altered between the two simulations. A comparison of estimated $\langle \overline{u}\overline{T} \rangle$ between NT and WT shows that the sub-tidal heat flux is reduced by 30%, not quite enough to account for the $\sim 40\%$ reduction noted in Table 1. Thus the remaining reduction is attributed to a net cooling by $\langle u'T' \rangle$. Additional conclusions are difficult to make without observations in deeper water, a mechanism-driven model of coastal tidal pumping, or a constraint on the effect of intrinsic stochastic variability associated with nonlinear coastal ocean models.

5 Summary

A realistic regional ocean model reproduces the observed coastal response of a northward-propagating, thermally-buoyant plume. Shelf-wide temperature increases during this event are primarily driven by lateral advective processes. In simulations with tides, temperature storage and advective heat fluxes are reduced by both a reduction in the low-frequency advective flux as well as a tidal pumping term which produces a net cooling of the shelf.

References

Chapman, D. C. (1985). Numerical Treatment of Cross-Shelf Open Boundaries in a Barotropic Coastal Ocean Model. *Journal of Physical Oceanography*, 15(8):1060–1075.

Flather, R. (1976). A tidal model of the northwest European continental shelf. *Mem. Soc. R. Sci. Liege*, 10(6):141–164.

Gill, A. E. (1982). *Atmosphere-ocean dynamics*. Academic Press.

Hodur, R., Hong, X., Doyle, J., Pullen, J., Cummings, J., Martin, P., and Rennick, M. A. (2002). The Coupled Ocean/Atmosphere Mesoscale Prediction System (COAMPS). *Oceanography*, 15(1):88–98.

Kumar, N., Feddersen, F., Suanda, S., Uchiyama, Y., and McWilliams, J. (2016). Mid- to inner-shelf coupled ROMS-SWAN model-data comparison of currents and temperature: Diurnal and semidiurnal variability. *Journal of Physical Oceanography*, pages 841–862.

Marchesiello, P., McWilliams, J. C., and Shchepetkin, A. (2001). Open boundary conditions for long-term integration of regional oceanic models. *Ocean modelling*, 3(1):1–20.

Mark, D. J., Spargo, E. A., Westerink, J. J., and Luettich, R. A. (2004). ENPAC 2003: A Tidal Constituent Database for Eastern North Pacific Ocean. Technical Report ERDC/CHL-TR-04-12, Coastal and Hydraul. Lab., U.S. Army Corps of Eng., Washington, D. C.

Mason, E., Molemaker, J., Shchepetkin, A. F., Colas, F., McWilliams, J. C., and Sangr, P. (2010). Procedures for offline grid nesting in regional ocean models. *Ocean Modelling*, 35(1):1–15.

Melton, C., Washburn, L., and Gotschalk, C. (2009). Wind relaxations and poleward flow events in a coastal upwelling system on the central California coast. *Journal of Geophysical Research: Oceans*, 114(C11):C11016.

Shchepetkin, A. F. and McWilliams, J. C. (2005). The regional oceanic modeling system (ROMS): a split-explicit, free-surface, topography-following-coordinate oceanic model. *Ocean Modelling*, 9(4):347–404.

Suanda, S. H. et al. (in revision 2016). Wind relaxation and a coastal buoyant plume north of Pt. Conception, CA: observations, simulations, and scalings. *Journal of Geophysical Research*.

Warner, J. C., Armstrong, B., He, R., and Zambon, J. B. (2010). Development of a Coupled Ocean–Atmosphere–Wave–Sediment Transport (COAWST) modeling system. *Ocean Modelling*, 35(3):230–244.

Washburn, L., Fewings, M. R., Melton, C., and Gotschalk, C. (2011). The propagating response of coastal circulation due to wind relaxations along the central California coast. *Journal of Geophysical Research: Oceans*, 116(C12):C12028.

Wilkin, J. L. (2006). The Summertime Heat Budget and Circulation of Southeast New England Shelf Waters. *Journal of Physical Oceanography*, 36(11):1997–2011.